

Article

Fast Initial Model Design for Electrical Resistivity Inversion by Using Broad Learning Framework

Tao Tao ¹, Peng Han ^{1,2,*}, Xiao-Hui Yang ³, Qiang Zu ¹, Kaiyan Hu ¹, Shuangling Mo ¹, Shuangshuang Li ¹, Qiang Luo ⁴ and Zhanxiang He ^{1,2}

- ¹ Department of Earth and Space Sciences, Southern University of Science and Technology, Shenzhen 518055, China; 12031167@mail.sustech.edu.cn (T.T.); zuqiang777@gmail.com (Q.Z.); huky@sustech.edu.cn (K.H.); mosl@mail.sustech.edu.cn (S.M.); 12331093@mail.sustech.edu.cn (S.L.); hezx@sustech.edu.cn (Z.H.)
- ² Guangdong Provincial Key Laboratory of Geophysical High-Resolution Imaging Technology, Southern University of Science and Technology, Shenzhen 518055, China
- ³ Plateau Atmosphere and Environment Key Laboratory of Sichuan Province, School of Atmospheric Sciences, Chengdu University of Information Technology, Chengdu 610225, China; yangxh@cuit.edu.cn
- ⁴ Guangdong Provincial Geophysical Prospecting Team, Guangzhou 510080, China; luoqiang595@126.com
- * Correspondence: hanp@sustech.edu.cn

Abstract: The electrical resistivity method is widely used in near-surface mineral exploration. At present, the deterministic algorithm is commonly employed in three-dimensional (3-D) electrical resistivity inversion to obtain subsurface electrical structures. However, the accuracy and efficiency of deterministic inversion rely on the initial model. In practice, obtaining an initial model that approximates the true subsurface electrical structures remains challenging. To address this issue, we introduce a broad learning (BL) network to determine the initial model and utilize the limited memory quasi-Newton (L-BFGS) algorithm to conduct the 3-D electrical resistivity inversion task. The powerful mapping capability of the BL network enables one to find the model that elucidates the actual observed data. The single-layer BL network makes it efficient and easy to realize, leading to much faster network training compared to that using the deep learning network. Both the synthetic and field experiments suggest that the BL framework could effectively obtain the initial model based on observed data. Furthermore, in comparison to using a homogeneous medium as the initial model, the L-BFGS inversion with the BL framework-designed initial model improves the inversion accuracy of subsurface electrical structures and expedites the convergence speed of the iteration. This study provides an effective approach for fast initial model design in a data-driven manner when the prior information is unavailable. The proposed method can be useful in high-precision imaging of near-surface mineral electrical structures.

Keywords: broad learning; 3-D electrical resistivity inversion; limited memory quasi-Newton; near-surface mineral exploration



Citation: Tao, T.; Han, P.; Yang, X.-H.; Zu, Q.; Hu, K.; Mo, S.; Li, S.; Luo, Q.; He, Z. Fast Initial Model Design for Electrical Resistivity Inversion by Using Broad Learning Framework. *Minerals* **2024**, *14*, 184. <https://doi.org/10.3390/min14020184>

Academic Editor: Stanisław Mazur

Received: 8 January 2024

Revised: 28 January 2024

Accepted: 3 February 2024

Published: 9 February 2024



Copyright: © 2024 by the authors. Licensee MDPI, Basel, Switzerland. This article is an open access article distributed under the terms and conditions of the Creative Commons Attribution (CC BY) license (<https://creativecommons.org/licenses/by/4.0/>).

1. Introduction

The electrical resistivity method is a well-known geophysical exploration method, holding significant value for various applications, including engineering surveys [1], environmental monitoring [2,3], mineral exploration [4–7], etc. The complex characteristics of underground structures are difficult to directly interpret using observed data imaging (e.g., apparent resistivity pseudosections). Thus, it is crucial to invert observed data to obtain accurate subsurface electrical structures. So far, various inversion techniques have been applied in electrical resistivity imaging studies, including global optimization, deterministic, and probabilistic methods [8]. Global optimization algorithms, such as simulated annealing [9], genetic algorithms [10,11], and particle swarm optimization [12], play a crucial role in solving optimization problems with multiple local optima by thoroughly

exploring the entire search space to identify the global optimum [13]. However, the high computational costs associated with global optimization algorithms limit their practical application in 3-D electrical resistivity inversion problems [11,14,15]. Deterministic methods such as the Gauss–Newton method [16], limited memory quasi-Newton method [17], and conjugate gradient method [18–21] are the popular approaches for the 3-D electrical resistivity inversion due to their promising performance in terms of result accuracy, stability, and convergence speed [8,11,22].

In the practical operation, deterministic inversion faces the challenge of selecting a suitable initial model for the inversion task [8,23]. Using an initial model that better represents the true underground electrical structures reduces the probability that inversion results fall into the local minima [24]. The use of a priori information is an effective approach for addressing the selection of the initial model [25,26], yet the deficiency of prior information is a common situation for underground electrical structure prospecting. As a result, a homogeneous initial resistivity model is principally considered in 3-D electrical resistivity inversion [27–31]. Additionally, the determination of the resistivity value for a homogeneous initial model also relies on the empirical selection [32]. Therefore, the selection of an appropriate initial model becomes a crucial issue in 3-D electrical resistivity deterministic inversion.

Machine learning (ML) applied to geophysical problems is a cutting-edge direction [33]. In recent years, ML has been utilized in many geophysics application areas, including pattern recognition in seismic attributes [34], noise removal [35,36], and inversion tasks [8,37–40]. As a representative of the ML, the deep learning (DL) network comes with strong learning and generalization capabilities, enabling excellent performance in electrical resistivity inversion problems [41–43]. However, the training procedures of DL suffer a time-consuming drawback induced by a mass of hyperparameters [44]. Meanwhile, to further improve the inversion effect, Kong et al. utilize the prediction results of DL as the initial model and reference model for the Gauss–Newton method [45]. But, it still has the problem of the high time cost caused by DL, especially in 3-D structural imaging. To overcome this drawback, Chen and Liu proposed the broad learning (BL) approach equipped with a single-layer network [44]. The training time for the deep learning network on the same training set may be hundreds of times longer than that of the BL network [44]. Recently, The BL network has been successfully applied in geophysical inversions, achieving noteworthy results [46–49]. These applications demonstrate that BL possesses the advantages of excellent efficiency and robust mapping capability.

Therefore, in this study, we introduced the BL network into the 3-D electrical resistivity inversion process. Firstly, the BL network is established based on the samples generated by forward calculation. Secondly, the initial model of 3-D electrical resistivity inversion is derived from observed data by using the constructed BL network. Finally, based on the designed initial resistivity model, the limited memory quasi-Newton (L-BFGS) algorithm is employed to undertake the 3-D electrical resistivity inversion task [17,50]. In the subsequent sections, the inversion results of both synthetic models and field applications are presented to verify the feasibility of the proposed method.

2. Materials and Methods

2.1. BL Framework for Initial Resistivity Model Design

To obtain the suitable initial resistivity model in 3-D electrical resistivity deterministic inversion, the BL network is employed to approximate the mapping relationship between the apparent resistivity data $\mathbf{x} \in \mathbb{R}^{N_x}$ (N_x is the number of apparent resistivity data) and the resistivity model $\mathbf{y} \in \mathbb{R}^{N_y}$ (N_y is the number of the resistivity model grid) as follows:

$$\mathbf{y} = \psi(\mathbf{x}), \quad (1)$$

where ψ is the functional mapping between apparent resistivity and the initial resistivity model to be simulated by the BL network.

Figure 1 shows the structure of the BL network for designing initial resistivity models. For the BL network training, the input $X \in \mathbb{R}^{N \times N_x}$ denotes the input apparent resistivity dataset, and the output $Y \in \mathbb{R}^{N \times N_y}$ reflects the output resistivity model dataset, where N represents the number of training samples. The following relationship is constructed to represent the target functional mapping ψ :

$$Y = [Z_1, \dots, Z_n, H_1, \dots, H_m]W = [Z, H]W, \tag{2}$$

where $Z = [Z_1, \dots, Z_n]$ is all the mapping features of the input apparent resistivity dataset X , and n is the number of groups of mapping features. Each group of mapping features with p neurons can be obtained by sparse autoencoder. $H = [H_1, \dots, H_m]$ is the number of the enhancement nodes derived from Z , and m is the number of groups of enhancement nodes. Each group of enhancement nodes is calculated by the nonlinear activation function as follows:

$$H_j = \varphi(ZW_j^H + \beta_j^H), \tag{3}$$

where W_j^H represents the j th random weight matrix; β_j^H represents the j th random bias vector, and H_j is the j th group of enhancement nodes. In this study, the $\tanh(\cdot)$ function is chosen as the nonlinear activation function. W is the only unknown matrix in the BL network, and it can be determined by the pseudoinverse as follows:

$$W = [Z, H]^+ Y = A^+ Y, \tag{4}$$

where $A = [Z, H]$. Particularly, the ridge regression algorithm is applied to solve the pseudoinverse A^+ [44].

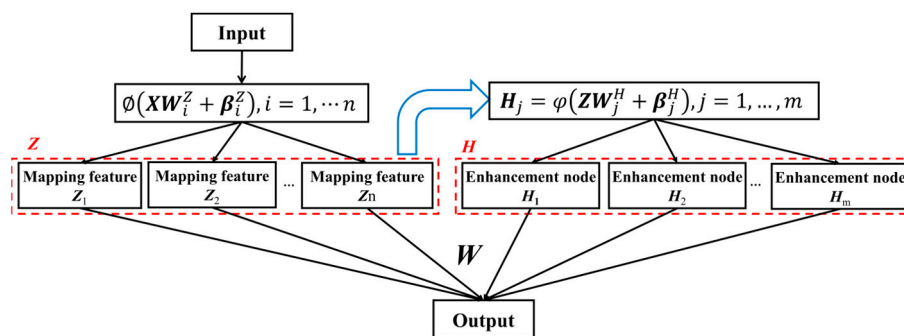


Figure 1. The BL network structure.

The BL network training is completed with the weighting matrix W determined for a given optimal network complexity (namely, a fixed combination of the parameters p , n , and m) [46]. Input the observed apparent resistivity data x into the trained BL network, and the initial resistivity model $\hat{y} \in \mathbb{R}^{N_y}$ can be designed:

$$\hat{y} = [Z', H']W, \tag{5}$$

where Z' is the mapping features of the apparent resistivity data $x \in \mathbb{R}^{N_x}$, and H' is the number of the corresponding enhancement nodes. For more detailed information about the BL network, please refer to [17].

2.2. Generation of Training Dataset

The BL is a supervised learning network that depends on a training dataset to learn the mapping relationship ψ . In this study, the training dataset is created through forward calculation and consists of the resistivity model (network output) and its corresponding apparent resistivity (network input). Specifically, the resistivity model is constructed

with a single cuboid anomalous body ‘A’ embedded in a homogeneous background ‘B’, as depicted in Figure 2a. The size and spatial position of anomalous body ‘A’ in each resistivity model are randomly generated. The resistivity values of ‘A’ and ‘B’ are randomly selected within a range from 1 to 500 Ω·m. Figure 2b illustrates the spatial distribution of observed apparent resistivity data for the resistivity model, calculated using the finite difference method.

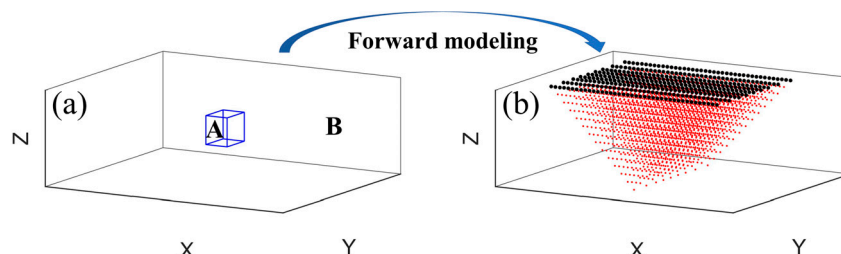


Figure 2. Schematic of a pair training sample. (a) Output resistivity model sample (‘A’ represents the regular anomalous body, and ‘B’ represents the background model). (b) Input apparent resistivity data sample (The black dots represent the locations of surface electrodes, while the red dots represent the spatial positions of apparent resistivity data points. Wenner arrays are adopted for visualization).

In the synthetic experiments, nine profiles are employed for data collection, each featuring 40 electrodes spaced 1 m apart. The data for each profile are acquired using the Wenner array, resulting in the collection of 247 data points. The model mesh is divided into 92 (X direction) × 84 (Y direction) × 29 (Z direction). In the survey line area, the minimum grid spacing of the resistivity model in the lateral direction is set to half of the electrode spacing. Beyond this region, the lateral grid spacing gradually increases with a factor of 1.3. For the first three layers in the vertical direction, the grid spacing is 0.1 m, and then it increases with a factor of 1.2.

2.3. Select of Training Dataset Size

The choice of training dataset size in the training phase depends on various factors, such as the complexity of the resistivity model to be predicted and the desired degree of precision [8]. Generally, a larger training dataset can help improve the performance and generalization ability of the network [8]. However, collecting an excessive number of training samples significantly increases the computation time consumption while providing minimal improvements in results [37]. Therefore, it is meaningful to choose the appropriate number of training samples.

To determine the appropriate training dataset size, we trained the BL using different training dataset sizes and evaluated the results using a validation dataset consisting of 500 samples that were not involved in the training process. Table 1 provides mean absolute percentage error (MAPE) at different training dataset sizes. As the size of the training dataset increases, the MAPE values of the training dataset and validation dataset gradually decrease. When the training dataset size is 12,000, both the training dataset and validation dataset have the minimum MAPE values, and the MAPE of the validation dataset does not decrease further compared to a training dataset size of 11,000. Therefore, to reduce the time spent on collecting training samples, we utilized the training dataset consisting of 12,000 samples to train the BL network.

Table 1. Training of BL network with different sizes of training datasets.

Number of Training Dataset	6000	8000	10,000	11,000	12,000
MAPE of the training dataset (%)	1.26	1.16	1.07	1.02	0.99
MAPE of the validation dataset (%)	1.06	1.04	1.03	1.02	1.02

2.4. Choose of BL Network Complexity

The complexity of the BL network is determined by the following three key factors: the number of feature nodes (p); the number of mapping groups (n); and the corresponding enhancement nodes (m). When these parameters are set to small values, the network structure becomes simple, which may not be able to efficiently extract features and result in poor mapping capability. On the other hand, if the network structure is too complex, it can lead to overfitting the training dataset [48]. Therefore, selecting an appropriate network complexity is crucial.

In this study, we select the appropriate network complexity by conducting an exhaustive search on these three parameters (p, n, m) within the range [50:50:200], [40:20:100], and [100:100:500], using 12,000 training samples and 500 validation samples. All samples are generated in the manner described in Section 2.2, and the validation dataset is not included in the training process. To assess the predictive accuracy of different network complexities, the deviation between the predicted resistivity model and the true one is calculated by the mean absolute percentage error (MAPE). When the p, n , and m are set to 200, 80, and 100, respectively, both the training and validation datasets exhibit the lowest MAPE values. Therefore, this study considers these three values as the optimal network complexity for the BL.

2.5. L-BFGS Inversion with Designed Initial Model

To circumvent the challenge of selecting the initial resistivity model in 3-D electrical resistivity deterministic inversion, we adopt the output result $\hat{\mathbf{y}}$ obtained from the BL framework as the initial resistivity model for the inversion task by using the L-BFGS algorithm, and the corresponding objective function is as follows:

$$\Gamma(\mathbf{y}) = (\mathbf{x} - f(\mathbf{y}))^T \mathbf{C}_x^{-1} (\mathbf{x} - f(\mathbf{y})) + \mu (\mathbf{y} - \mathbf{y}_{ref})^T \mathbf{C}_y^{-1} (\mathbf{y} - \mathbf{y}_{ref}), \quad (6)$$

where \mathbf{x} denotes the apparent resistivity data used for the inversion; \mathbf{y} is the inverted resistivity model at each iteration, with the initial resistivity model being the output result $\hat{\mathbf{y}}$ of the BL framework; $f(\cdot)$ is the forward calculation operator, and \mathbf{C}_x is the data covariance matrix, which takes into account the relative importance of the observations [51]. To avoid the inversion process from focusing on fitting large values in the observed data, the observed data are employed to construct the data covariance matrix. The superscript T represents the transpose operation; \mathbf{y}_{ref} is the homogeneous reference model whose resistivity value is given by the mode of the designed initial model vector $\hat{\mathbf{y}}$; \mathbf{C}_y is the model covariance matrix; and μ is the regularization parameter. For the details of the L-BFGS algorithm, readers can refer to [17,52,53]. The inversion process using the designed initial model is concisely outlined as follows:

1. Set fitting tolerance error ζ and a maximum number of iterations Num . Input apparent resistivity data \mathbf{x} and the designed initial resistivity model $\hat{\mathbf{y}}$;
2. Calculate the apparent resistivity data \mathbf{x}^{cal} of the current k th iteration resistivity model \mathbf{y}_k by forward modeling: $\mathbf{x}^{cal} = f(\mathbf{y}_k)$;
3. Calculate the partial derivative $\nabla \Gamma(\mathbf{y}_k, \mathbf{x})$ of Equation (6), and calculate the search direction \mathbf{p}_k . Obtain the appropriate step α_k by line search and update resistivity model $\mathbf{y}_{k+1} = \mathbf{y}_k + \alpha_k \mathbf{p}_k$;
4. Compute the misfit between observed data \mathbf{x} and calculated data \mathbf{x}^{cal} . If misfit $< \zeta$ or $k > Num$ inversion stop; otherwise, set $k = k + 1$ and go to step 2.

3. Results

In this section, four synthetic examples and a field experiment are used to assess the performance of 3-D electrical resistivity inversion based on the initial model designed by a BL framework. In addition to qualitatively evaluating the inversion results through visual judgment, we perform the quantitative evaluation on the final inversion results using

the $MAPE = \frac{1}{N_y} \sum_{i=1}^{N_y} \left| \frac{y_i - \hat{y}_i}{y_i} \right|$ (where \hat{y} represents the final inversion result) and assess the data misfit using the normalized root-mean-error $NRMSE = \sqrt{\frac{1}{N_x} \sum_{i=1}^{N_x} \left(\frac{x_i - \hat{x}_i}{x_i} \right)^2}$ (where \hat{x} represents the apparent resistivity data obtained through the forward calculation of the inversion model). In this study, the initial resistivity model design is conducted on a workstation equipped with a 3.80 GHz Intel Xeon W-2235 CPU.

3.1. Synthetic Experiment 1

Synthetic experiment 1 tests the performance of the 3-D electrical resistivity inversion with the designed initial model using a single regular anomalous body model (Figure 3a). It consists of a 10 $\Omega \cdot m$ rectangular prism embedded in a 100 $\Omega \cdot m$ homogeneous medium. The dimensions of the rectangular prism are 4 m (length) \times 8 m (width) \times 2 m (height), with its top located at a depth of 3 m. The spatial heterogeneity of the synthetic resistivity model is determined by multiple profiles aligned in parallel along the y-direction (Figure 3a, black dots). Figure 3b shows the initial resistivity model designed by the BL framework, with training and prediction times of 207 s and 0.5 s, respectively. The designed initial model approximately captures the structure of the anomalous body.

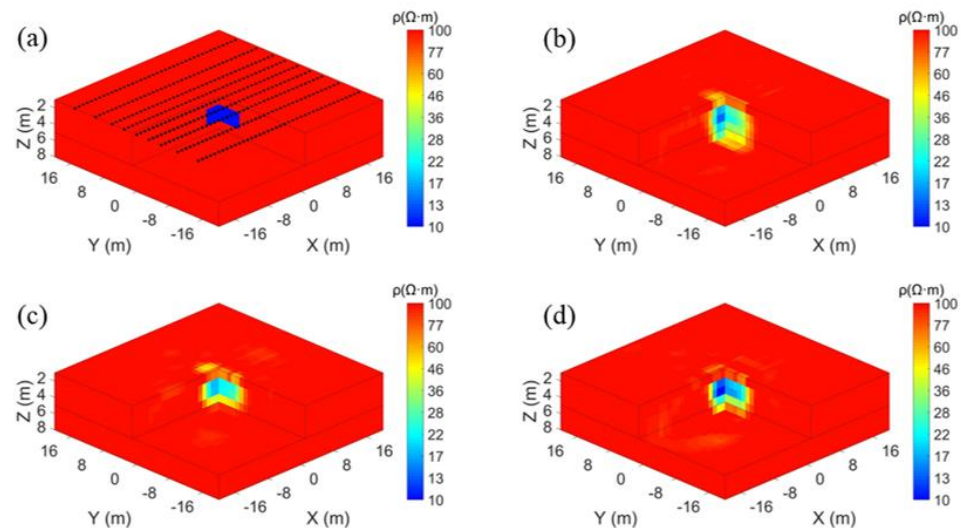


Figure 3. Synthetic model and inversion results. (a) The synthetic model. The black dots represent the positions of surface electrodes; nine profiles are deployed. (b) The initial resistivity model is designed by the BL framework. (c,d) The L-BFGS inversion results using the homogeneous initial model and the designed initial model, respectively.

Figure 3c illustrates the inversion result of the L-BFGS algorithm using the homogeneous initial model (inversion time approximately 115 min). It delineates the shape of the anomalous body, but there are redundant structures at the top interface of the anomalous body, which can be misinterpreted as the anomalous extending to the surface. Figure 3d shows the L-BFGS inversion result using the initial resistivity model designed by the BL framework (inversion time approximately 110 min). Comparing Figure 3c with Figure 3d, it is evident that Figure 3d effectively suppresses redundant structures on the upper boundary of the anomalous body, leading to a more accurate delineation of the anomalous body boundary. Furthermore, the $MAPE$ values of the L-BFGS inversion results for those two initial models are 2.62% (homogeneous initial model) and 2.35% (designed initial model), respectively. It indicates that the inversion result using the proposed method is more accurate compared to the traditional method.

The $NRMSE$ value (0.31%) of the first iteration of the proposed method corresponds to the $NRMSE$ value of the designed initial model. However, after 100 iterations, the data misfit ($NRMSE = 0.11\%$) using the traditional method is smaller than directly using the output of the BL network (the designed initial model). It indicates that the designed initial

model fits the data less effectively than the inversion results of the homogeneous initial model. We, thereby, used the outputting model of the trained BL network as the initial model for further L-BFGS inversion.

Figure 4 displays the *NRMSE* curves of the L-BFGS method utilizing two different initial models. The *NRMSE* value achieved by the proposed method is consistently lower than that obtained by the traditional method at the same iteration number. For example, after 35 iterations of the L-BFGS method utilizing the designed initial model, the *NRMSE* value is smaller than the *NRMSE* value obtained by the traditional method after 100 iterations. This test demonstrates the capacity of the initial model crafted by a BL network to enhance the convergence speed of deterministic inversion.

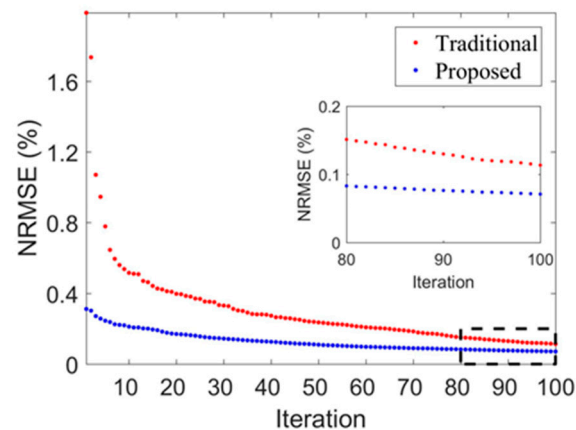


Figure 4. *NRMSE* curves of L-BFGS inversion shown in Figure 3 using the homogeneous initial model and the designed initial model, respectively. The red dots indicate the homogeneous medium as the initial resistivity model (Traditional). The blue dots indicate the initial resistivity model designed by the BL framework (Proposed).

3.2. Synthetic Experiment 2

In many cases, the distribution of the electrical property of the underlying geology exhibits an irregular structure. Hence, this section utilizes an irregular anomaly body model to assess the proposed method. The background and anomaly resistivity values are set at $50 \Omega \cdot \text{m}$ and $100 \Omega \cdot \text{m}$, respectively. The irregular anomaly body is positioned approximately as a parallelogram on the horizontal plane and is situated at a depth ranging from 4 m to 7 m underground. For a clearer visual representation of the irregular anomaly body's shape, Figure 5a depicts the true model slices at various depths ($[Z = 4 \text{ m}, 5 \text{ m}, 6 \text{ m}, 7 \text{ m}]$). Figure 5b displays the initial model slices generated by the BL network. The total training and prediction time of the BL network is within 4 min. While the resistivity values of the anomaly body may not precisely match the true value of $100 \Omega \cdot \text{m}$, the shape of the anomaly body closely resembles that of the true model. Figure 5c illustrates slices of the L-BFGS inversion result using the homogeneous initial model (inversion time of approximately 129 min). It inadequately delineates both the value and shape of the anomaly body and the accuracy of the inversion result degrades with an increase in the depth of the anomaly body. Furthermore, the structural details of the anomaly body are not clearly discernible at depths between 6 m and 7 m. Figure 5d exhibits slices of the L-BFGS inversion result utilizing the initial model designed by the BL network (inversion time of approximately 102 min). An evident high-resistivity anomalous body is discerned at depths ranging from 3 m to 7 m, corresponding to the actual anomaly body area. The *MAPE* values of the L-BFGS inversion results for the two initial models are 1.91% (homogeneous initial model) and 1.28% (designed initial model), respectively. Consequently, the subsurface resistivity structure presented in Figure 5d is deemed more realistic in comparison to the L-BFGS inversion result using the homogeneous initial model (Figure 5c). The results suggest that utilizing the designed initial model can improve the accuracy of electrical resistivity inversion.

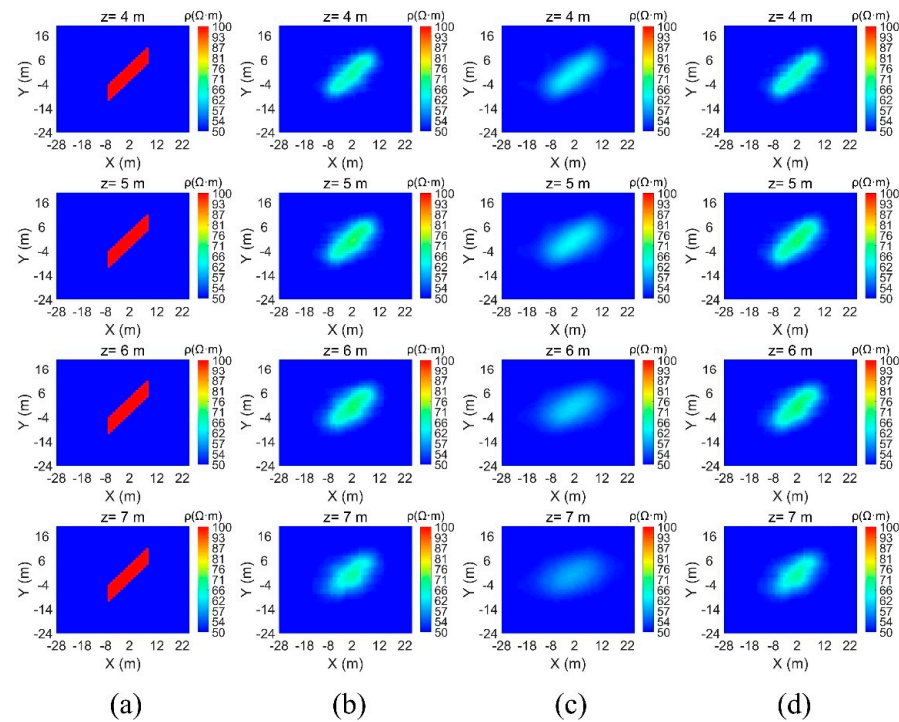


Figure 5. Synthetic model slices, designed initial model slices, and inversion results slices. By row, from top to bottom: the slices at a depth of 4 m, 5 m, 6 m, and 7 m, respectively. By the column, from left to right: (a) The synthetic model slices; (b) The initial model slices are designed by the BL framework; (c) The inversion result slices of L-BFGS using the homogeneous initial model; (d) The inversion result slices of L-BFGS inversion using the designed initial model. Note: The resistivity model in the training dataset contains only one regular anomaly body, and the resistivity values of both the anomaly and the model background are random numbers between 1 and 500 Ω -m.

The *NRMSE* curves of the L-BFGS inversion for two different initial models are shown in Figure 6, and the *NRMSE* value for inversion using the designed initial model decreases more rapidly than that of the homogeneous initial model inversion. Specifically, at 13 inversion iterations, the *NRMSE* value using the designed initial model is smaller than the *NRMSE* value at 100 inversion iterations using the homogeneous initial model.

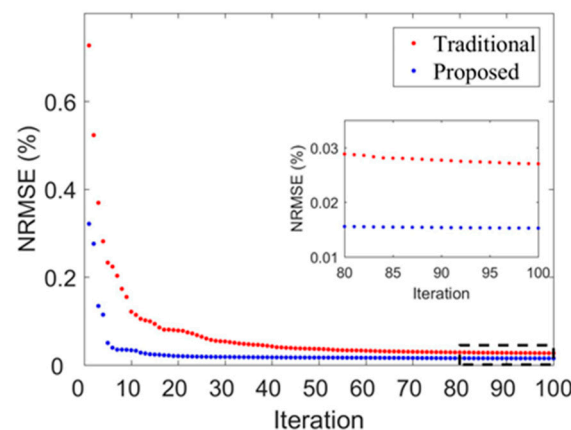


Figure 6. *NRMSE* curves of L-BFGS inversion shown in Figure 5 using the homogeneous initial model and the designed initial model, respectively. The red dots indicate the homogeneous medium as the initial resistivity model (Traditional). The blue dots indicate the initial resistivity model designed by the BL framework (Proposed).

This synthetic example illustrates that the BL network, trained on single regular model samples, can effectively design the initial model for irregular underground electrical structures. Moreover, employing the designed initial model in electrical resistivity inversion can enhance the convergence speed of the inversion process.

3.3. Synthetic Experiment 3

In practice, subsurface electrical structures may contain multiple anomalous bodies. Therefore, we consider a complex synthetic model to test the generalization of the proposed method. The synthetic model consists of three $10 \Omega \cdot \text{m}$ conductive rectangular prisms and three $400 \Omega \cdot \text{m}$ resistive rectangular prisms embedded in a $100 \Omega \cdot \text{m}$ homogeneous medium. All six prisms are located 3 m to 5 m below the surface, as shown in Figure 7a. It is important to note that the resistivity model in the training dataset is a single regular anomaly body, and the model with multiple anomalies is not included. The total training and prediction time of the BL network is within 4 min (Training (218 s), Prediction (0.6 s)). Figure 7b shows the initial resistivity model designed by the BL framework. It roughly delineates the electrical structures of the true model, showing that the training dataset only contains a single anomalous body and can also perform initial model design for electrical structures with multiple anomalous bodies.

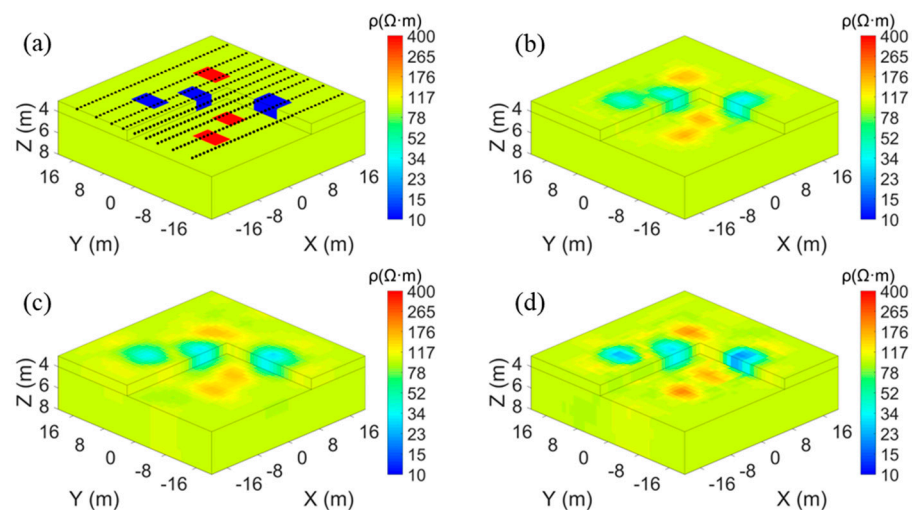


Figure 7. Synthetic model and inversion results. (a) The synthetic model. (b) The initial model. (c,d) The L-BFGS inversion results using the homogeneous initial model and the designed initial model, respectively. Note: The resistivity model in the training dataset contains only one regular anomaly body, and the resistivity values of both the anomaly and the model background are random numbers between 1 and $500 \Omega \cdot \text{m}$.

Figure 7c,d displays the L-BFGS inversion results using the homogeneous initial model (inversion time of approximately 116 min) and the designed initial model (inversion time of approximately 93 min), respectively. Compared to Figure 7c, Figure 7d shows better recovery of the values and shape of the anomalous bodies. Furthermore, the *MAPE* values for the L-BFGS inversion results using the homogeneous initial model (Traditional) and the designed initial model (Proposed) are 4.97% and 4.30%, respectively. This indicates that the inversion result obtained using the proposed method is closer to the true model compared to the traditional method.

We also show the *NRMSE* curves of the L-BFGS inversion for two different initial resistivity models in Figure 8. The results indicate that the *NRMSE* values using the proposed method are much smaller than those of the traditional method under the same iteration number.

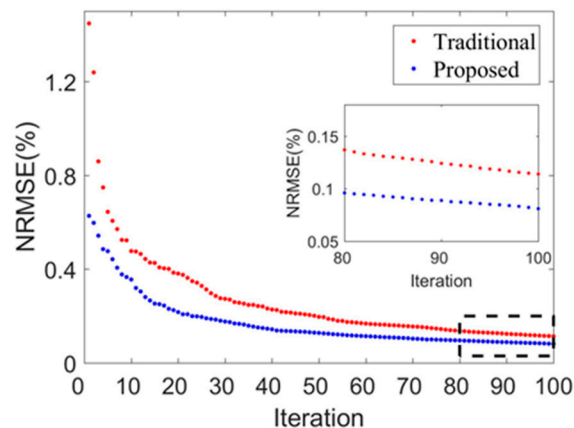


Figure 8. NRMSE curves of the L-BFGS inversion shown in Figure 7 using the homogeneous initial model (Traditional) and the designed initial model (Proposed), respectively. The red dots indicate the homogeneous medium as the initial resistivity model (Traditional). The blue dots indicate the initial resistivity model designed by the BL framework (Proposed).

3.4. Synthetic Experiment 4

In this section, a complex synthetic model, as illustrated in Figure 9a, is employed to evaluate the proposed method. The synthetic model comprises a 100 Ω·m rectangular prism and a 300 Ω·m irregular resistive anomalous body embedded in a 200 Ω·m homogeneous half-space. The depth of the anomaly bodies ranges from 3 m to 5 m, with the high-conductive body surrounded by the high-resistive body on three faces. The initial model designed through the Broad Learning (BL) framework is illustrated in Figure 9b, and the corresponding training and prediction times are 200 s and 0.5 s, respectively. It approximately depicts structures of high and low resistivity anomalies that resemble the characteristics of the actual model. The L-BFGS inversion results using the homogeneous initial model and the designed initial model are presented in Figure 9c (inversion time of approximately 122 min) and Figure 9d (inversion time of approximately 106 min), respectively. In comparison with the inversion result in Figure 9c (MAPE 1.11%), the result obtained with the designed initial model (Figure 9d) (MAPE 0.81%) more accurately characterizes the value and shape of anomaly bodies.

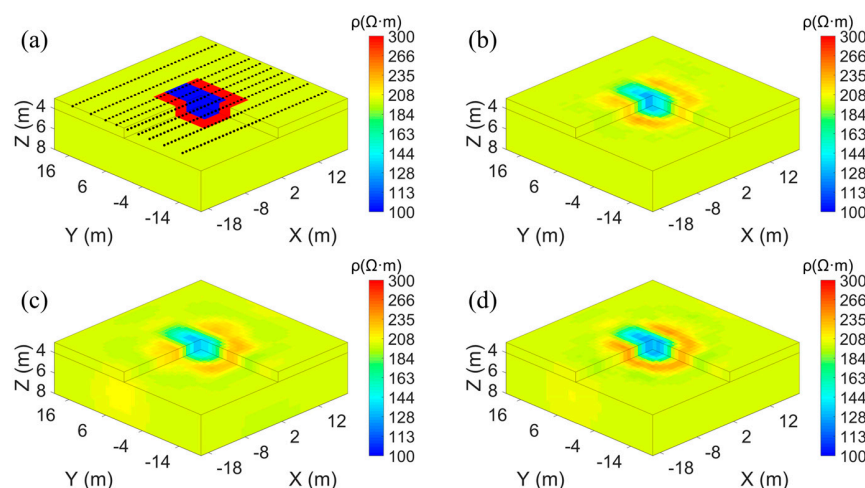


Figure 9. Synthetic model, designed initial model, and inversion results. (a) Synthetic model. (b) The initial model is designed by the BL framework. (c) The L-BFGS inversion result using the homogeneous initial model. (d) The L-BFGS inversion result using the designed initial model. Note: The resistivity model in the training dataset contains only one regular anomaly body, and the resistivity values of both the anomaly and the model background are random numbers between 1 and 500 Ω·m.

Figure 10 illustrates the *NRMSE* curves of the L-BFGS method with the two different initial models. The *NRMSE* value from the inversion using the designed initial model is smaller than the *NRMSE* value of the homogeneous initial model inversion at the same number of iterations. Specifically, at 54 iterations, the *NRMSE* value using the designed initial model is smaller than the *NRMSE* value at 100 iterations of the homogeneous initial model inversion.

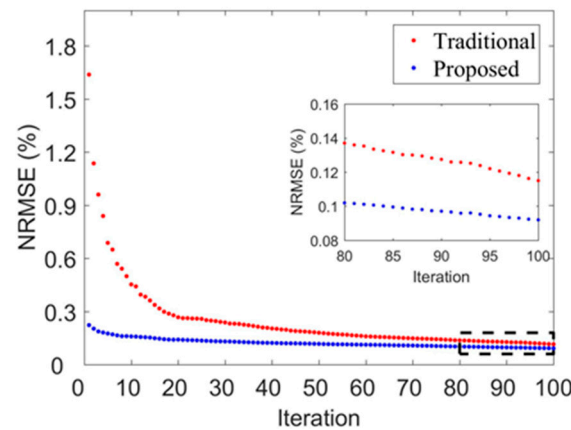


Figure 10. *NRMSE* curves of the L-BFGS inversion shown in Figure 9 using the homogeneous initial model (Traditional) and the designed initial model (Proposed), respectively. The red dots indicate the homogeneous medium as the initial resistivity model (Traditional). The blue dots indicate the initial resistivity model designed by the BL framework (Proposed).

3.5. Field Experiment

In addition, we conduct a field experiment in a farmland area south of Shenzhen, China. In the experimental area, we carried out three profiles with 1.5 m profile spacing, as shown in Figure 11a. For each profile, 20 electrodes are laid out with an electrode interval of 0.4 m. We bury an empty foam box (high resistivity) (Figure 11c) of 0.3 m (length) \times 0.27 m (width) \times 0.2 m (height) under the No. 5 electrode of profile P1. Its top interface is 0.1 m below the ground surface. In addition, we bury an iron box (high conductivity) (Figure 11b) with a size of 0.42 m (length) \times 0.3 m (width) \times 0.28 m (height) under No. 10 and No. 11 electrodes of profile P2; the top interface of the iron box is approximately 0.05 m from the surface, and the long side is parallel to the survey profile. The standard Wenner configuration is used for the survey. The model mesh is divided into $67 \times 51 \times 23$. Setting the electrode spacing to less than half the size of the targets could enhance the spatial resolution of electrical resistivity exploration.

A high-resistivity anomalous body in the No. 5 electrode region of profile P1 and a low-resistivity anomalous body in the middle of profile P2 can be observed in the initial resistivity model designed by the BL framework (Figure 12a). These two resistivity anomalous bodies correspond to the foam box and the iron box, respectively. However, there are redundant structures at the bottom of the anomalous bodies.

The L-BFGS inversion results after 10 iterations, employing the homogeneous initial model (inversion time approximately 24 min) and the designed initial model (inversion time approximately 22 min), are presented in Figures 12b and 12c, respectively. Compared with the inversion result in Figure 12b, the result in Figure 12c shows a clearer characterization of the foam box and iron box. The *NRMSE* curves in Figure 12d also indicate that the L-BFGS inversion using the designed initial resistivity model fits the observed apparent resistivity data better than the homogeneous initial model. This field experiment demonstrates that higher inversion accuracy can be obtained based on the designed initial resistivity model using the BL framework rather than directly using L-BFGS inversion.

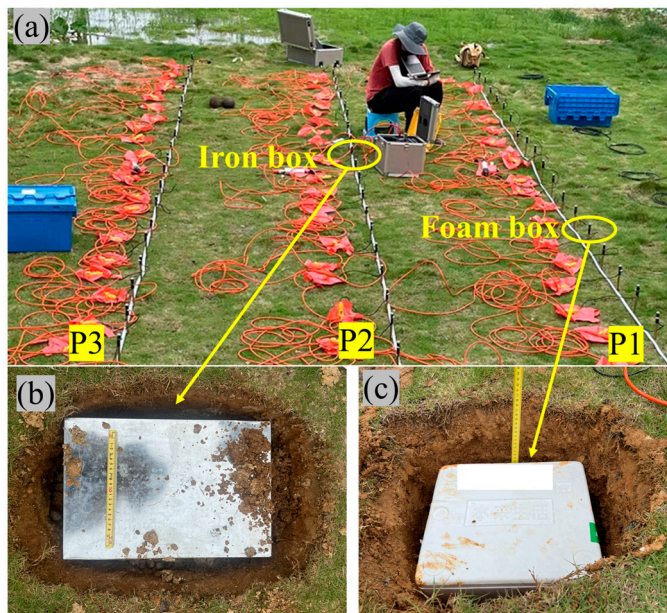


Figure 11. Schematic of the field area. (a) A photo shows the three profiles of the field site. P1, P2, and P3 represent profile 1, profile 2, and profile 3, respectively. (b) The photo shows the iron box under profile P2. (c) The photo shows the foam box under profile P1.

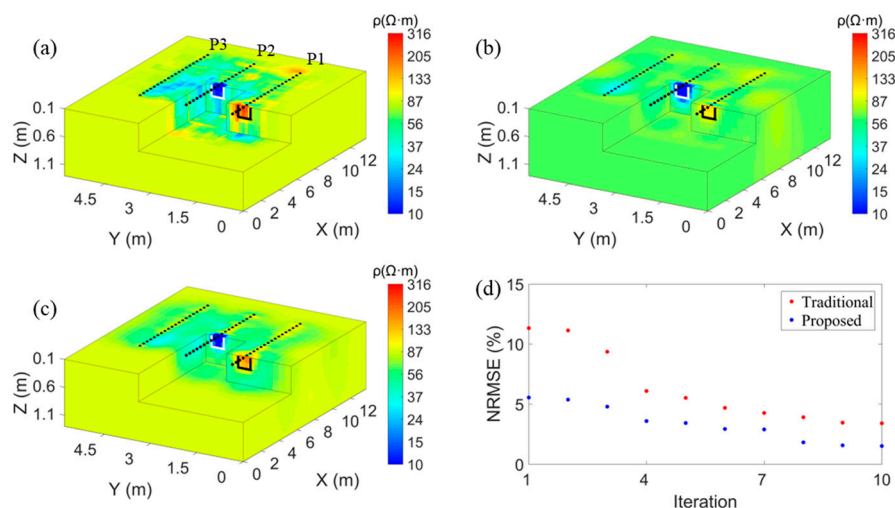


Figure 12. Inversion results and iteration *NRMSE* curves. The white rectangle indicates the location of the iron box, and the black rectangle indicates the location of the foam box. (a) The initial model. (b) The L-BFGS inversion result using the homogeneous initial model. (c) The L-BFGS inversion result using the designed initial model. (d) The *NRMSE* curves of the L-BFGS inversion using the homogeneous initial model (Traditional) and the designed initial model (Proposed), respectively. Note: The resistivity model in the training dataset contains only one regular anomaly body, and the resistivity values of both the anomaly and the model background are random numbers between 1 and 500 $\Omega \cdot m$.

4. Discussion

4.1. Generalization Ability of BL Network

Synthetic experiments showcase the generalization ability of the BL network in characterizing both multiple anomalous electrical bodies and irregular anomalous bodies. In these experiments, all earth model samples used for training the BL network are of resistivity values within the range of (1, 500) $\Omega \cdot m$. However, in practical operation, the resistivity values of earth models can surpass this range. To assess the generalization capability of the

BL network, we test it with five earth models having resistivity values exceeding 500 Ω·m. The five synthetic models are depicted in the left column of Figure 13, and the specific parameter values of the models are detailed in Table 2. The right column of Figure 13 displays the predicted results using the BL network trained before (the samples within the range of (1, 500) Ω·m). The BL network can still effectively delineate the structural characteristics of the true subsurface model. Notably, the BL network can design an accurate initial model, even when the resistivity values of the models exceed the training dataset.

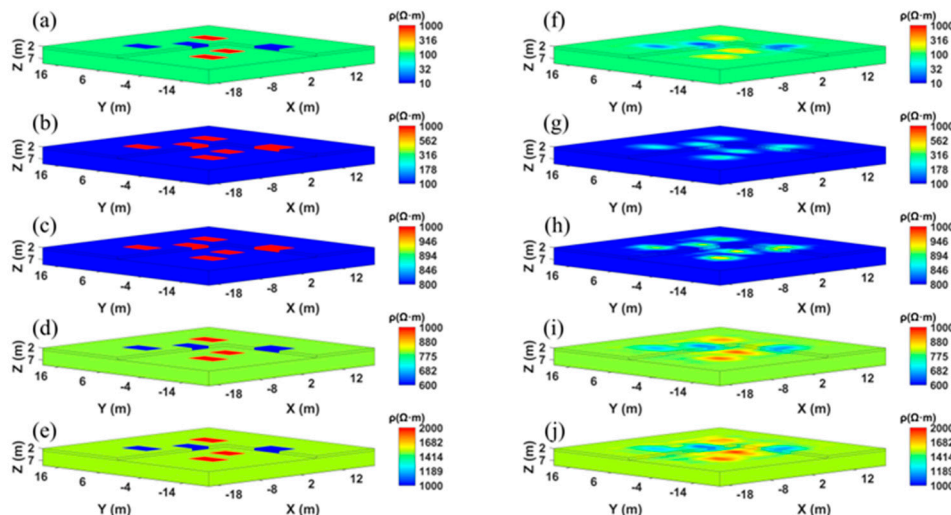


Figure 13. Synthetic models and initial models. (a–e) The synthetic models. The resistivity values corresponding to the true models are presented in Table 2. (f–j) The initial model designed by the BL network. Note: The resistivity model in the training dataset contains only one regular anomaly body, and the resistivity values of both the anomaly and the model background are random numbers between 1 and 500 Ω·m.

Table 2. The resistivity values of synthetic models.

Synthetic Model	Low Resistivity	High Resistivity	Background Resistivity	MAPE (%)
(a)	10 Ω·m	1000 Ω·m	100 Ω·m	4.34
(b)		1000 Ω·m	100 Ω·m	3.12
(c)		1000 Ω·m	800 Ω·m	0.43
(d)	600 Ω·m	1000 Ω·m	800 Ω·m	0.51
(e)	1000 Ω·m	2000 Ω·m	1500 Ω·m	0.98

4.2. Noise Resistance Test

In practice, observation data are often contaminated by noise. To assess the impact of noise on the proposed method, we add 20% Gaussian random noise ($noise_i = x_i \times 20\% \times r_i$; x_i represents i th observed apparent resistivity data, and r_i represents the Gaussian random number) to the apparent resistivity data of Experiment 1. Figure 14a shows the initial resistivity model designed by the BL framework, which contains a noticeable false anomaly in the background. Figure 14b shows the L-BFGS inversion result using the initial resistivity model designed by the BL framework. Compared with the result in Figure 14a, the redundant structures in Figure 14b are significantly reduced, and the anomalous body is closer to the true model. As shown in Figure 14a, although the input data are contaminated and changed by the noise, the BL network can still provide useful information about the anomalous body. Compared with the result shown in Figure 3b, the mapping accuracy decreased when relatively strong noise (20%) existed. Therefore, we use the output result of the BL framework as the initial resistivity model for deterministic inversion to further improve the accuracy of the inversion result.

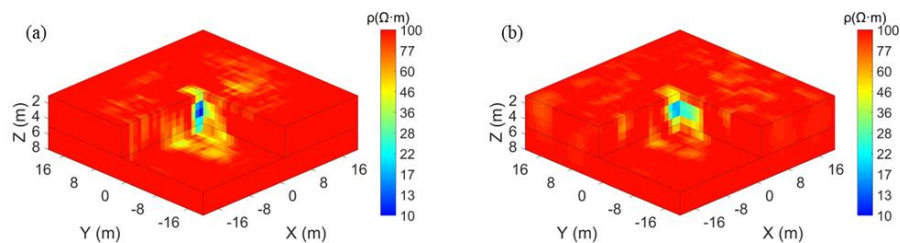


Figure 14. Initial resistivity model and inversion result. (a) The initial resistivity model is designed by the BL framework. (b) The L-BFGS inversion result uses the initial resistivity model designed by the BL framework.

The impact of noise is an important issue for field data. Noise within the field data diminishes the precision of inversion results, consequently impeding the accurate identification of authentic anomalies. To enhance the accuracy of imaging results, we plan to integrate denoising methods with the proposed inversion technique in future work.

4.3. Checkerboard Test

To further verify the reliability of the field experiment results, we employ the checkerboard test to analyze the resolution of the inversion results. The checkerboard model is depicted in Figure 15a. The background resistivity value is 50 $\Omega \cdot m$, with the low-resistance anomaly at 10 $\Omega \cdot m$ and the high-resistivity anomaly at 100 $\Omega \cdot m$. The sizes of the low-resistance anomaly and the high-resistivity anomaly are both 0.4 m (length) \times 0.4 m (width) \times 0.2 m (height). The intervals between the anomaly bodies in the X direction and Y direction are 1 m and 0.8 m, respectively. Figure 15b presents the initial model designed through the BL network. In the whole region, the initial model designed by the BL network could approximately represent the pattern of the anomaly, although in regions lacking measuring points some redundant structures existed. Figure 15c depicts the inversion result obtained through the L-BFGS algorithm using a homogeneous initial model. Below the survey line, the inversion result reproduces the structure of the anomaly bodies. However, beyond the coverage area of the survey line, the inversion result fails to depict the anomaly bodies. Figure 15d shows the inversion result obtained through the L-BFGS algorithm using the designed initial model. Compared Figure 15c with Figure 15d, it is evident that Figure 15d gives a more accurate delineation of the anomaly bodies. The *NRMSE* curves of the L-BFGS inversion for two different initial models are depicted in Figure 16. The *NRMSE* value for inversion using the designed initial model decreases more rapidly than that of the homogeneous initial model inversion. Specifically, at 27 inversion iterations, the *NRMSE* value using the designed initial model is smaller than that at 100 inversion iterations using the homogeneous initial model.

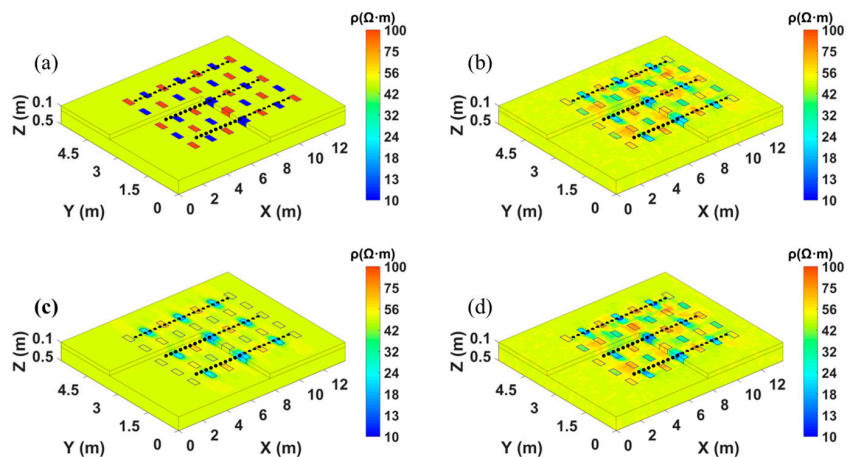


Figure 15. Synthetic model and inversion results. The black dots represent the locations of the electrodes on the surface. (a) The synthetic model. The black dots represent the positions of surface electrodes; nine

profiles are deployed. (b) The initial resistivity model is designed by the BL framework. (c,d) The L-BFGS inversion results using the homogeneous initial model and the designed initial model, respectively. Note: The resistivity model in the training dataset contains only one regular anomaly body, and the resistivity values of both the anomaly and the model background are random numbers between 1 and 500 $\Omega\cdot\text{m}$.

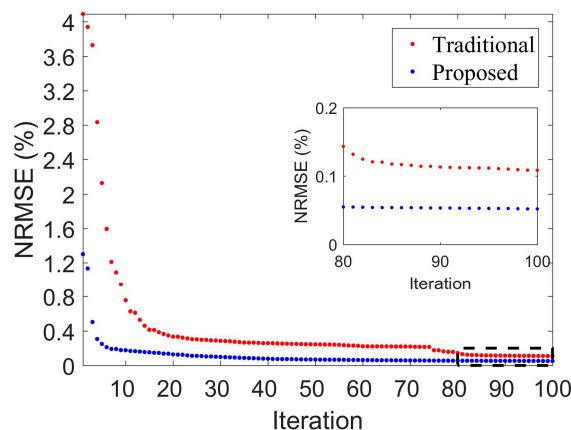


Figure 16. NRMSE curves of L-BFGS inversion shown in Figure 15 using the homogeneous initial model and the designed initial model, respectively. The red dots indicate the homogeneous medium as the initial resistivity model (Traditional). The blue dots indicate the initial resistivity model designed by the BL framework (Proposed).

Different arrays demonstrate varying sensitivities to underground structures, and the choice of observation arrays should align with specific problem requirements, such as signal-to-noise ratio and horizontal or vertical resolutions. In this study, the Wenner array, selected for its high signal-to-noise ratio, is employed to test the proposed method. The BL network trained in this article is only suitable for the given observation strategy. In the practical operation, the parameters, including observation arrays, the number of observation data, survey line spacing, and electrode spacing to generate the training dataset, should be set the same as field observation. For measurement data with different observation arrays or containing multiple observation arrays, a new training set needs to be constructed for network training.

5. Conclusions

The initial model selection is crucial and challenging in 3-D electrical resistivity deterministic inversion. In this study, we introduce the Broad Learning (BL) framework for fast initial model design and employ the L-BFGS algorithm for the 3-D electrical resistivity inversion task. The BL framework is constructed based on the training dataset consisting of only one regular anomaly body, yet it could provide a reliable and effective initial resistivity model, even though the underground electrical structure may contain multiple anomalous bodies. Synthetic and field experiments verify the effectiveness of the BL framework in designing the initial resistivity model. Furthermore, in comparison to the homogeneous initial resistivity model, the L-BFGS inversion using the initial resistivity model designed by the BL framework can increase the convergence speed and improve the accuracy of the inversion result. This study provides a useful tool for the initial resistivity model design in deterministic inversion and can be helpful in high-precision imaging of electrical structures.

Metallic minerals typically exhibit lower resistivities compared to non-metallic minerals or surrounding rocks. This contrast in resistivity values enables the identification of mineralized zones through electrical resistivity exploration. The proposed inversion method in this study facilitates the high-precision imaging of subsurface electrical structures, en-

abling geologists and geophysicists to better delineate and understand the distribution of mineralized zones.

Author Contributions: Conceptualization, T.T., X.-H.Y. and P.H.; methodology, T.T., X.-H.Y. and P.H.; investigation, T.T., X.-H.Y. and P.H.; data curation, Q.Z., S.M. and S.L.; writing—original draft preparation, T.T.; writing—review and editing, T.T., X.-H.Y., K.H. and P.H.; visualization, T.T., X.-H.Y., K.H. and P.H.; supervision, Q.L., Z.H. and P.H.; project administration, P.H.; funding acquisition, P.H. All authors have read and agreed to the published version of the manuscript.

Funding: This research is partly supported by the National Key Research and Development Program of China (Grant No. 2022YFF0800601), Science and Technology Program of Shenzhen (Grant No. JCYJ20210324104602006), Guangdong Provincial Key Laboratory of Geophysical High-resolution Imaging Technology (Grant No. 2022B1212010002).

Data Availability Statement: The associated data and codes used by this study are available at the link <https://github.com/TaoTao-geophysics/BL-network-design-initial-model> accessible from 8 January 2024.

Acknowledgments: We extend our sincere gratitude to C. L. Philip Chen and Zhulin Liu for generously providing the broad learning code. We also wish to express our appreciation to Rui Wang, Hongyan Chen, Zhiyi Zeng, and Peijie Wang for their valuable discussions throughout this study.

Conflicts of Interest: The authors declare no conflicts of interest.

References

- Cardarelli, E.; Cercato, M.; Di Filippo, G. Geophysical investigation for the rehabilitation of a flood control embankment. *Near Surf. Geophys.* **2010**, *8*, 287–296. [CrossRef]
- Ibraheem, I.M.; Tezkan, B.; Bergers, R. Integrated interpretation of magnetic and ERT data to characterize a landfill in the north-west of Cologne, Germany. *Pure Appl. Geophys.* **2021**, *178*, 2127–2148. [CrossRef]
- Yu, N.; Liu, H.; Feng, X.; Li, T.; Du, B.; Wang, C.; Wang, W.; Kong, W. Advancing CO₂ Storage Monitoring via Cross-Borehole Apparent Resistivity Imaging Simulation. *IEEE Trans. Geosci. Remote Sens.* **2023**, *61*, 1–12. [CrossRef]
- Ali, M.A.H.; Mewafy, F.M.; Qian, W.; Alshehri, F.; Ahmed, M.S.; Saleem, H.A. Integration of Electrical Resistivity Tomography and Induced Polarization for Characterization and Mapping of (Pb-Zn-Ag) Sulfide Deposits. *Minerals* **2023**, *13*, 986. [CrossRef]
- Uhlemann, S.; Chambers, J.; Falck, W.E.; Tirado Alonso, A.; Fernández González, J.L.; de Gea, A.E. Applying electrical resistivity tomography in ornamental stone mining: Challenges and solutions. *Minerals* **2018**, *8*, 491. [CrossRef]
- Shin, Y.; Shin, S.; Cho, S.-J.; Son, J.-S. Application of 3D Electrical Resistivity Tomography in the Yeoncheon Titanomagnetite Deposit, South Korea. *Minerals* **2021**, *11*, 563. [CrossRef]
- Su, Z.; Revil, A.; Ghorbani, A.; Zhang, X.; Zhao, X.; Richard, J. Combining Electrical Resistivity, Induced Polarization, and Self-Potential for a Better Detection of Ore Bodies. *Minerals* **2023**, *14*, 12. [CrossRef]
- Vu, M.; Jardani, A. Convolutional neural networks with SegNet architecture applied to three-dimensional tomography of subsurface electrical resistivity: CNN-3D-ERT. *Geophys. J. Int.* **2021**, *225*, 1319–1331. [CrossRef]
- Sharma, S.P. VFSARES—A very fast simulated annealing FORTRAN program for interpretation of 1-D DC resistivity sounding data from various electrode arrays. *Comput. Geosci.* **2012**, *42*, 177–188. [CrossRef]
- Başokur, A.T.; Akca, I. Object-based model verification by a genetic algorithm approach: Application in archeological targets. *J. Appl. Geophys.* **2011**, *74*, 167–174. [CrossRef]
- Liu, B.; Li, S.; Nie, L.; Wang, J.; Zhang, Q. 3D resistivity inversion using an improved Genetic Algorithm based on control method of mutation direction. *J. Appl. Geophys.* **2012**, *87*, 1–8. [CrossRef]
- Barboza, F.M.; Medeiros, W.E.; Santana, J.M. A user-driven feedback approach for 2D direct current resistivity inversion based on particle swarm optimization Feedback inversion using PSO. *Geophysics* **2019**, *84*, E105–E124. [CrossRef]
- Sosa, A.; Velasco, A.A.; Velazquez, L.; Arguez, M.; Romero, R. Constrained optimization framework for joint inversion of geophysical data sets. *Geophys. J. Int.* **2013**, *195*, 1745–1762. [CrossRef]
- Aleardi, M.; Vinciguerra, A.; Hojat, A. A convolutional neural network approach to electrical resistivity tomography. *J. Appl. Geophys.* **2021**, *193*, 104434. [CrossRef]
- Alyousuf, T.; Li, Y. Inversion using adaptive physics-based neural network: Application to magnetotelluric inversion. *Geophys. Prospect.* **2022**, *70*, 1252–1272. [CrossRef]
- Pidlisecky, A.; Haber, E.; Knight, R. RESINVM3D: A 3D resistivity inversion package. *Geophysics* **2007**, *72*, H1–H10. [CrossRef]
- Wu, P.; Tan, H.; Tao, T.; Ma, H.; Ding, Z.; Xu, L. Three-dimensional joint inversion of the resistivity method and ambient noise method with cross-gradient constraints. *Chin. J. Geophys.* **2020**, *63*, 3912–3930.
- Wu, X.; Xu, G. Study on 3-D resistivity inversion using conjugate gradient method. *Chin. J. Geophys.* **2000**, *43*, 450–458.
- Peng, M.; Tan, H.; Moorkamp, M. Structure-coupled 3-D imaging of magnetotelluric and wide-angle seismic reflection/refraction data with interfaces. *J. Geophys. Res. Solid Earth* **2019**, *124*, 10309–10330. [CrossRef]

20. Kong, W.; Tan, H.; Lin, C.; Unsworth, M.; Lee, B.; Peng, M.; Wang, M.; Tong, T. Three-Dimensional Inversion of Magnetotelluric Data for a Resistivity Model with Arbitrary Anisotropy. *J. Geophys. Res. Solid Earth* **2021**, *126*, e2020JB020562. [[CrossRef](#)]
21. Xu, L.; Tan, H.; Wu, P.; Peng, M.; Wang, S.; Jiang, M. Electrical characteristics of the crust in the south part of Longmenshan fault zone: Evidence from magnetotelluric inversion with velocity structure constraints. *Chin. J. Geophys.* **2022**, *65*, 3434–3450.
22. Ma, H.; Guo, Y.; Wu, P.; Tan, H. 3-D joint inversion of multi-array data set in the resistivity method based on MPI parallel algorithm. *Chin. J. Geophys.* **2018**, *61*, 5052–5065.
23. Wilson, B.; Singh, A.; Sethi, A. Appraisal of Resistivity Inversion Models with Convolutional Variational Encoder–Decoder Network. *IEEE Trans. Geosci. Remote Sens.* **2022**, *60*, 1–10. [[CrossRef](#)]
24. Yuval, D.; Oldenburg, W. DC resistivity and IP methods in acid mine drainage problems: Results from the Copper Cliff mine tailings impoundments. *J. Appl. Geophys.* **1996**, *34*, 187–198. [[CrossRef](#)]
25. Wunderlich, T.; Fischer, P.; Wilken, D.; Hadler, H.; Erkul, E.; Mecking, R.; Günther, T.; Heinzlmann, M.; Vött, A.; Rabbel, W. Constraining electric resistivity tomography by direct push electric conductivity logs and vibracores: An exemplary study of the Fiume Morto silted riverbed (Ostia Antica, western Italy). *Geophysics* **2018**, *83*, B87–B103. [[CrossRef](#)]
26. Pidlisecky, A.; Knight, R.; Haber, E. Cone-based electrical resistivity tomography. *Geophysics* **2006**, *71*, G157–G167. [[CrossRef](#)]
27. Loke, M.H.; Barker, R.D. Rapid least-squares inversion of apparent resistivity pseudosections by a quasi-Newton method1. *Geophys. Prospect.* **1996**, *44*, 131–152. [[CrossRef](#)]
28. Günther, T.; Rücker, C.; Spitzer, K. Three-dimensional modelling and inversion of DC resistivity data incorporating topography—II. Inversion. *Geophys. J. Int.* **2006**, *166*, 506–517. [[CrossRef](#)]
29. Wagner, F.; Mollaret, C.; Günther, T.; Kemna, A.; Hauck, C. Quantitative imaging of water, ice and air in permafrost systems through petrophysical joint inversion of seismic refraction and electrical resistivity data. *Geophys. J. Int.* **2019**, *219*, 1866–1875. [[CrossRef](#)]
30. Palacios, A.; Ledo, J.J.; Linde, N.; Luquot, L.; Bellmunt, F.; Folch, A.; Marcuello, A.; Queralt, P.; Pezard, P.A.; Martínez, L. Time-lapse cross-hole electrical resistivity tomography (CHERT) for monitoring seawater intrusion dynamics in a Mediterranean aquifer. *Hydrol. Earth Syst. Sci.* **2020**, *24*, 2121–2139. [[CrossRef](#)]
31. Goebel, M.; Knight, R.; Kang, S. Enhancing the resolving ability of electrical resistivity tomography for imaging saltwater intrusion through improvements in inversion methods: A laboratory and numerical study. *Geophysics* **2021**, *86*, WB101–WB115. [[CrossRef](#)]
32. Slezak, K.; Jozwiak, W.; Nowozynski, K.; Orynski, S.; Brasse, H. 3-D studies of MT data in the Central Polish Basin: Influence of inversion parameters, model space and transfer function selection. *J. Appl. Geophys.* **2019**, *161*, 26–36. [[CrossRef](#)]
33. Mousavi, S.M.; Beroza, G.C. Deep-learning seismology. *Science* **2022**, *377*, eabm4470. [[CrossRef](#)] [[PubMed](#)]
34. Qi, J.; Zhang, J.; Lyu, B.; Marfurt, K.J. Seismic Geometric Nonparallelism Attributes. *IEEE Geosci. Remote Sens. Lett.* **2020**, *19*, 1–5. [[CrossRef](#)]
35. Wu, S.; Huang, Q.; Zhao, L. De-noising of transient electromagnetic data based on the long short-term memory-autoencoder. *Geophys. J. Int.* **2021**, *224*, 669–681. [[CrossRef](#)]
36. Xue, J.; Huang, Q.; Wu, S.; Nagao, T. LSTM-Autoencoder Network for the Detection of Seismic Electric Signals. *IEEE Trans. Geosci. Remote Sens.* **2022**, *60*, 1–12. [[CrossRef](#)]
37. Wu, S.; Huang, Q.; Zhao, L. Convolutional neural network inversion of airborne transient electromagnetic data. *Geophys. Prospect.* **2021**, *69*, 1761–1772. [[CrossRef](#)]
38. Wu, S.; Huang, Q.; Zhao, L. Instantaneous inversion of airborne electromagnetic data based on deep learning. *Geophys. Res. Lett.* **2022**, *49*, e2021GL097165. [[CrossRef](#)]
39. Wu, S.; Huang, Q.; Zhao, L. Fast Bayesian Inversion of Airborne Electromagnetic Data Based on the Invertible Neural Network. *IEEE Trans. Geosci. Remote Sens.* **2023**, *61*, 1–11. [[CrossRef](#)]
40. Zhang, C.; Li, J.; Yu, H.; Liu, B. Autoencoded Elastic Wave-Equation Traveltime Inversion: Toward Reliable Near-Surface Tomogram. *IEEE Trans. Geosci. Remote Sens.* **2023**, *61*, 1–13. [[CrossRef](#)]
41. Liu, B.; Guo, Q.; Li, S.; Liu, B.; Ren, Y.; Pang, Y.; Guo, X.; Liu, L.; Jiang, P. Deep learning inversion of electrical resistivity data. *IEEE Trans. Geosci. Remote Sens.* **2020**, *58*, 5715–5728. [[CrossRef](#)]
42. Liu, B.; Pang, Y.; Jiang, P.; Liu, Z.; Liu, B.; Zhang, Y.; Cai, Y.; Liu, J. Physics-Driven Deep Learning Inversion for Direct Current Resistivity Survey Data. *IEEE Trans. Geosci. Remote Sens.* **2023**, *61*, 1–11. [[CrossRef](#)]
43. Li, Y.; Yang, D. Electrical imaging of hydraulic fracturing fluid using steel-cased wells and a deep-learning method Electrical hydraulic fracturing imaging. *Geophysics* **2021**, *86*, E315–E332. [[CrossRef](#)]
44. Chen, C.P.; Liu, Z. Broad learning system: An effective and efficient incremental learning system without the need for deep architecture. *IEEE Trans. Neural Netw. Learn. Syst.* **2017**, *29*, 10–24. [[CrossRef](#)]
45. Kong, S.; Oh, J.; Yoon, D.; Ryu, D.-W.; Kwon, H.-S. Integrating Deep Learning and Deterministic Inversion for Enhancing Fault Detection in Electrical Resistivity Surveys. *Appl. Sci.* **2023**, *13*, 6250. [[CrossRef](#)]
46. Yang, X.-H.; Han, P.; Yang, Z.; Miao, M.; Sun, Y.-C.; Chen, X. Broad Learning Framework for Search Space Design in Rayleigh Wave Inversion. *IEEE Trans. Geosci. Remote Sens.* **2022**, *60*, 1–17. [[CrossRef](#)]
47. Yang, X.-H.; Han, P.; Yang, Z.; Chen, X. Two-stage broad learning inversion framework for shear-wave velocity estimation. *Geophysics* **2023**, *88*, WA219–WA237. [[CrossRef](#)]

48. Hu, K.; Ren, H.; Huang, Q.; Zeng, L.; Butler, K.E.; Jougnot, D.; Linde, N.; Holliger, K. Water Table and Permeability Estimation from Multi-Channel Seismoelectric Spectral Ratios. *J. Geophys. Res. Solid Earth* **2023**, *128*, e2022JB025505. [[CrossRef](#)]
49. Zhou, Y.; Li, X.; Tang, Q.; Kuok, S.C.; Fei, K.; Gao, L. An Assimilating Model Using Broad Learning System for Incorporating Multi-Source Precipitation Data with Environmental Factors Over Southeast China. *Earth Space Sci.* **2022**, *9*, e2021EA002043. [[CrossRef](#)]
50. Byrd, R.H.; Lu, P.; Nocedal, J.; Zhu, C. A limited memory algorithm for bound constrained optimization. *SIAM J. Sci. Comput.* **1995**, *16*, 1190–1208. [[CrossRef](#)]
51. Colombo, D.; Turkoglu, E.; Li, W.; Sandoval-Curiel, E.; Rovetta, D. Physics-driven deep-learning inversion with application to transient electromagnetics. *Geophysics* **2021**, *86*, E209–E224. [[CrossRef](#)]
52. Nocedal, J. Updating quasi-Newton matrices with limited storage. *Math. Comput.* **1980**, *35*, 773–782. [[CrossRef](#)]
53. Wang, T.; Wang, K.-P.; Tan, H.-D. Forward modeling and inversion of tensor CSAMT in 3D anisotropic media. *Appl. Geophys.* **2017**, *14*, 590–605. [[CrossRef](#)]

Disclaimer/Publisher’s Note: The statements, opinions and data contained in all publications are solely those of the individual author(s) and contributor(s) and not of MDPI and/or the editor(s). MDPI and/or the editor(s) disclaim responsibility for any injury to people or property resulting from any ideas, methods, instructions or products referred to in the content.